Supplementary Materials for

Elevated dust layers inhibit dissipation of heavy anthropogenic surface air pollution

Zhuang Wang[1,2], Cheng Liu[2,3,1,5,6*], Zhouqing Xie[4,3,1,6*] ,Qihou Hu[1*], Meinrat O. Andreae[7,8], Yunsheng Dong[1], Chun Zhao[4], Ting Liu[4], Yizhi Zhu[1,2], Haoran Liu[10], Chengzhi Xing[1,4], Wei Tan[1,2], Xiangguang Ji[9], Jinan Lin[1,2], Jianguo Liu[1,3]

[1]Key Lab of Environmental Optics & Technology, Anhui Institute of Optics and Fine Mechanics, Chinese Academy of Sciences, Hefei, 230031, China.

[2]Department of Precision Machinery and Precision Instrumentation, University of Science and Technology of China, Hefei, 230026, China.

[3]Center for Excellence in Regional Atmospheric Environment, Institute of Urban Environment, Chinese Academy of Sciences, Xiamen, 361021, China.

[4]School of Earth and Space Sciences, University of Science and Technology of China, Hefei, 230026, China.

[5]Key Laboratory of Precision Scientific Instrumentation of Anhui Higher Education Institutes, University of Science and Technology of China, Hefei, 230026, China.

[6]Anhui Province Key Laboratory of Polar Environment and Global Change, University of Science and Technology of China, Hefei, 230026, China.

[7]Max Planck Institute for Chemistry, Mainz, 55128, Germany.

[8]Department of Geology and Geophysics, King Saud University, 11451 Riyadh, Saudi Arabia.

[9]School of Environmental Science and Optoelectronic Technology, University of Science and Technology of China, Hefei, 230026, China.

[10]Institute of Physical Science and Information Technology, Anhui University, Hefei, 230601, China.

Correspondence to: Cheng Liu (chliu81@ustc.edu.cn), Zhouqing Xie (zqxie@ustc.edu.cn), Qihou Hu (qhhu@aiofm.ac.cn)

Section S1. Inversion method and data verification of RL parameters

Lidar ratio (LR) at 355 nm. Aerosol LR ($S_{\lambda_o}^{aer}$) is defined as the aerosol extinction–to–backscatter ratio ($S_{\lambda_o}^{aer}(z_o)=\alpha_{\lambda_o}^{aer}(z_o)/\beta_{\lambda_o}^{aer}(z_o)$). The aerosol extinction coefficients ($\alpha_{\lambda_o}^{aer}$) and backscatter coefficients ($\beta_{\lambda_o}^{aer}$) at 355 nm were calculated from the elastic and inelastic return signals (Ansmann et al., 1990; Ansmann et al., 1992b). We assumed particle scattering to be proportional to λ^{-k} with the value of k=1 for pollution aerosol (Ansmann et al., 2005) and k=0 for dust (Ansmann et al., 1992a). The nitrogen molecule number density, atmospheric molecule extinction, and atmospheric molecule backscatter were derived from a standard atmosphere model. Only nighttime (from 18:00 to 06:00 local time) data were used to compute the LR due to the large daytime background noise. Moreover, 10–point spatial smoothing and three–hour averaging for the nitrogen Raman signal were used to reduce the relative error in computing the LR (Fig. S4). The overlap function

(Wandinger and Ansmann, 2002) must be used to determine the LR in the lower lidar layer, it was computed under clear conditions.

Volume depolarization ratio (VDR) at 532 nm. VDR is defined as the ratio of the perpendicular polarized signal to the parallel polarized signal (Freudenthaler et al., 2009; Murayama et al., 1999). This method can obtain accurate VDR values without assuming the reference value in the atmosphere, but a calibration experiment must be implemented regularly (Freudenthaler et al., 2009).

Aerosol extinction coefficient at 355 nm (EXT_{355}). As the signal–to–noise ratio of the inelastic backscatter Raman signal was extremely low during daytime, only the elastic backscatter signal was available and thus the Fernald method (Klett, 1981; Fernald, 1984) had to be used to retrieve the EXT_{355}. This method requires two crucial assumptions, a reference value of the EXT_{355} as in the inelastic method and the range–dependent LR, which may cause greater errors under heavy pollution conditions (Sasano et al., 1985). To obtain accurate values of the EXT_{355}, a reasonable evaluation of the range–dependent LR is necessary. Considering that the vertical structure of aerosols in the same heavy pollution incident has similar characteristics, we used the nighttime average LR to represent the daytime values. In addition, a 10–point spatial smoothing average for the elastic backscatter signal was used to reduce the relative error in computing the EXT_{355}.

Aerosol extinction coefficient at 532 nm (EXT_{532}). The total elastic backscatter signal (Ansmann et al., 1992a) profile at 532 nm was used to compute the EXT_{532}, which is defined as $P_{532}(z)=P_{532p}(z)+P_{532s}(z)$. The retrieval method is the same as that using the elastic backscatter signal to compute the EXT_{355}, but the LR at 355 nm was set equal to the LR at 532 nm (Sugimoto et al., 2002). This assumption may introduce additional errors due to the wavelength dependence of LR (Groß et al., 2015; Groß et al., 2017). Thus, the EXT_{355} was used to analyze the air pollution status during the observation period.

Water vapor mixing ratio. The water vapor mixing ratio can be defined as the ratio of water vapor mass to the dry air mass within a certain volume. The water vapor mixing ratio m(z) can be derived by detecting the Raman signal of water vapor (Whiteman et al., 1992; Behrendt et al., 2002)

$$m(z)=c_m * \Delta q_m(z_0,z) * \frac{I_H(z)}{I_Z(z)} \quad (1)$$

Where z is the height; c_m is the system calibration constant; Δq_m is the transmission correction function; and I_H and I_N are the inelastic backscatter Raman signals of water vapor and nitrogen, respectively. A 10–point spatial smoothing and hourly average for the water vapor and nitrogen Raman signal were used to calculate the water mixing ratio to reduce relative error. Relative humidity (RH) can be obtained by combining the water vapor mixing ratio m(z) measured by RL and the temperature and pressure profile simulated by the Weather Research and Forecasting (WRF) model coupled with Chemistry (WRF–Chem) model. We needed to spline–interpolate the spatial resolution of temperature and pressure profile to 7.5 m due to the different spatial resolution between WRF–Chem model and RL.

The water vapor sounding experiment was conducted on 16 Aug 2017 at the Beijing Observatory near Beijing's South

Fifth Ring (39°48′23″ N, 116°28′03″ E). The RH comparison of the RL and radiosonde is provided in Fig. S5, which shows that the RL and radiosonde were consistent in measuring RH at noon and night.

Data comparison. Besides RL, multi–axis differential optical absorption spectroscopy (MAX–DOAS) was performed since Jan 2017. Figure S5 shows the EXT_{355} comparison of RL and MAX–DOAS during our observation period. The hourly and spatially average EXT from 400 m to 600 m and 600 m to 800 m were selected due to the blind zone of RL and different spatial resolution between RL (7.5 m) and MAX–DOAS (100 m). In general, the EXT comparisons of RL and MAX–DOAS show a reasonably good agreement ($R > 0.8$). Because the sensitivity of the MAX–DOAS measurements decreases with increasing altitude in the troposphere (Frieß et al., 2006), the slope of linear regression between RL and MAX–DOAS measured EXT is less than 1. In addition, MAX–DOAS and lidar measurements were made with different geometries (a combination of zenith–sky and off–axis versus zenith–sky only, respectively) and different integration times for completing a set of measurements (15 versus 22 min, respectively), which may also explain part of the differences (Irie et al., 2008).

In addition, the seasonal average vertical structure of EXT_{532} and depolarization ratio was compared with the Cloud–Aerosol Lidar and Infrared Pathfinder Satellite Observations (CALIPSO) lidar. The CALIPSO satellite provides the vertical structure of global aerosols since Jun 2006. The system emits linearly polarized light at 532 and 1064 nm, and simultaneously receives 532 nm parallel and cross–polarized backscatter signals. A complete overview of the architecture and performance of CALIPSO and the data retrieval algorithms can be found in Hunt et al., 2009 and Winker et al., 2009, respectively. The CALIPSO level 2 aerosol profile products ("CAL_LID_L2_05kmAPro–Prov–V3–40"), including extinction coefficient at 532 nm and particulate depolarization ratio (PDR) at 532 nm, are used for comparison. It is difficult to expect aerosols in the planetary boundary layer to be similarly distributed over a long distances (Anderson et al., 2003). Thus, only CALIPSO overpasses that occurred at a distance of less than 150 km and a temporal difference of less than 1h were selected. A total number of 18 overpasses from 23 Jan to 29 Mar 2017 was found, 15 qualified for comparison. Details of the 15 cases used for comparison are listed in Table S1. Figure S6 provides a comparison of three–month average aerosol extinction coefficient and depolarization ratio (PDR for CALIPSO and VDR for RL) vertical structure between RL and CALIPSO satellite measurements. We also calculated the relative bias to quantify the comparison by the following equation:

$$\text{Bias}(z)=100\% * \frac{\delta_{\text{CALIPSO}}(z)-\delta_{\text{RL}}(z)}{\delta_{\text{CALIPSO}}(z)} \quad (2)$$

Where z is the height, δ is the EXT_{532} or depolarization ratio measured by RL and CALIPSO. Generally, the three–month average comparison results are in reasonable agreement with such efforts over other parts of the world (Pappalardo et al., 2010; Tesche et al., 2013).

Section S2. WRF–Chem simulations verification

To ensure the accuracy of the WRF–Chem model, the key meteorology parameters, including temperature, relative humidity, and wind speed/direction were compared with radiosonde data (http://weather.uwyo.edu/, last access: 6 Jan 2020) at Beijing (39.93 °N, 116.28 °E, WMO station number 54511). The radiosondes were launched twice a day (08:00 and 20:00 LT) and measured profiles of atmospheric variables such as air temperature, water mixing ratio, wind speed, etc. As shown in Fig.

S7, the WRF–Chem model can effectively reproduce the meteorology parameters. Observed hourly surface–layer $PM_{2.5}$ concentrations from 21 Jan to 6 Feb 2017 at Chengde (40.97 ºN, 117.82 ºE, station number 1065A), Zhangjiakou (40.81 ºN, 114.88 ºE, station number 1059A), Beijing (40.14 ºN, 116.72 ºE, station number 1008A), Tianjing (39.03 ºN, 117.71 ºE, station number 1023A), Baoding (38.88 ºN, 115.44 ºE, station number 1055A), Cangzhou (38.30 ºN, 116.89 ºE, station number 1071A), Shijiazhuang (38.14 ºN, 114.50 ºE, station number 1031A), and Hengshui (37.73 ºN, 115.69 ºE, station number 1076A) were compared with the model results from the dust_on case (Fig. S8). The observed $PM_{2.5}$ values were downloaded from the environmental monitoring station (http://beijingair.sinaapp.com/, last access: 5 January 2020). Generally, the WRF–Chem model can reasonably reproduce the evolutional characteristics of the observed $PM_{2.5}$ concentrations in the eight cities (Li et al., 2016; Wang et al., 2019; Gao et al., 2016) (R: 0.52–0.81). Both the observed and simulated $PM_{2.5}$ concentrations exhibit a heavy pollution period from 22 to 26 Jan 2017 and 1 to 5 Feb 2017.

References

Anderson, T. L., Charlson, R. J., Winker, D. M., Ogren, J. A., and Holmén, K.: Mesoscale variations of tropospheric aerosols, J. Atmos. Sci., 60, 119-136, doi: 10.1175/1520-0469(2003)060<0119:MVOTA>2.0.CO;2, 2003.

Ansmann, A., Engelmann, R., Althausen, D., Wandinger, U., Hu, M., Zhang, Y., He, Q.: High aerosol load over the Pearl River Delta, China, observed with Raman lidar and Sun photometer, Geophys. Res. Lett., 32, L13815, doi: 10.1029/2005gl023094, 2005.

Ansmann, A., Riebesell, M., and Weitkamp, C.: Measurement of atmospheric aerosol extinction profiles with a Raman lidar, Opt. Lett., 15, 746-748, doi: 10.1364/OL.15.000746, 1990.

Ansmann, A., Riebesell, M., Wandinger, U., Weitkamp, C., Voss, E., Lahmann, W., and Michaelis, W.: Combined Raman elastic-backscatter lidar for vertical profiling of moisture, aerosol extinction, backscatter, and lidar ratio, Appl. Phys. B, 55, 18-28, 1992a.

Ansmann, A., Wandinger, U., Riebesell, M., Weitkamp, C., and Michaelis, W.: Independent measurement of extinction and backscatter profiles in cirrus clouds by using a combined Raman elastic-backscatter lidar, Appl. Opt., 31, 7113-7131, doi: 10.1364/AO.31.007113, 1992b.

Behrendt, A., Nakamura, T., Onishi, M., Baumgart, R., and Tsuda, T.: Combined Raman lidar for the measurement of atmospheric temperature, water vapor, particle extinction coefficient, and particle backscatter coefficient, Appl. Opt., 41, 7657-7666, doi: 10.1364/AO.41.007657, 2002.

Fernald, F. G.: Analysis of atmospheric lidar observations: some comments, Appl. Opt., 23, 652-653, doi: 10.1364/AO.23.000652, 1984.

Freudenthaler, V., Esselborn, M., Wiegner, M., Heese, B., Tesche, M., Ansmann, A., MüLler, D., Althausen, D., Wirth, M., Fix, A., Ehret, G., Knippertz, P., Toledano, C., Gasteiger, J., Garhammer, M., and Seefeldner, M.: Depolarization ratio profiling at several wavelengths in pure Saharan dust during SAMUM 2006, Tellus B, 61, 165-179, doi: 10.1111/j.1600-0889.2008.00396.x, 2009.

Frieß, U., Monks, P. S., Remedios, J. J., Rozanov, A., Sinreich, R., Wagner, T., and Platt, U.: MAX-DOAS O4 measurements: A new technique to derive information on atmospheric aerosols: 2. Modeling studies, J. Geophys. Res., 111, D14203 doi: 10.1029/2005jd006618, 2006.

Gao, M., Carmichael, G. R., Wang, Y., Saide, P. E., Yu, M., Xin, J., Liu, Z., and Wang, Z.: Modeling study of the 2010 regional haze event in the North China Plain, Atmos. Chem. Phys., 16, 1673-1691, doi: 10.5194/acp-16-1673-2016, 2016.

Groß, S., Freudenthaler, V., Wirth, M., and Weinzierl, B.: Towards an aerosol classification scheme for future EarthCARE lidar observations and implications for research needs, Atmos. Sci. Lett., 16, 77-82, doi: 10.1002/asl2.524, 2015.

Groß, S., Tesche, M., Freudenthaler, V., Toledano, C., Wiegner, M., Ansmann, A., Althausen, D., and Seefeldner, M.: Characterization of Saharan dust, marine aerosols and mixtures of biomass-burning aerosols and dust by means of multi-wavelength depolarization and Raman lidar measurements during SAMUM 2, Tellus B, 63, 706-724, doi: 10.1111/j.1600-0889.2011.00556.x, 2017.

Heese, B., Flentje, H., Althausen, D., Ansmann, A., and Frey, S.: Ceilometer lidar comparison: backscatter coefficient retrieval

and signal-to-noise ratio determination, Atmos. Meas. Tech., 3, 1763-1770, doi: 10.5194/amt-3-1763-2010, 2010.
Hunt, W. H., Winker, D. M., Vaughan, M. A., Powell, K. A., Lucker, P. L., and Weimer, C.: CALIPSO Lidar Description and Performance Assessment, J. Atmos. Oceanic Technol., 26, 1214-1228, doi: 10.1175/2009jtecha1223.1, 2009.
Irie, H., Kanaya, Y., Akimoto, H., Iwabuchi, H., Shimizu, A., and Aoki, K.: First retrieval of tropospheric aerosol profiles using MAX-DOAS and comparison with lidar and sky radiometer measurements, Atmos. Chem. Phys., 8, 341-350, doi: 10.5194/acp-8-341-2008, 2008.
Klett, J. D.: Stable analytical inversion solution for processing lidar returns, Appl. Opt., 20, 211-220, doi: 10.1364/AO.20.000211, 1981.
Li, T., Wang, H., Zhao, T., Xue, M., Wang, Y., Che, H., and Jiang, C.: The Impacts of Different PBL Schemes on the Simulation of PM2.5during Severe Haze Episodes in the Jing-Jin-Ji Region and Its Surroundings in China, Adv. Meteorol., 2016, 1-15, doi: 10.1155/2016/6295878, 2016.
Murayama, T., Okamoto, H., Kaneyasu, N., Kamataki, H., and Miura, K.: Application of lidar depolarization measurement in the atmospheric boundary layer: Effects of dust and sea-salt particles, J. Geophys. Res. Atmos., 104, 31781-31792, doi: 10.1029/1999jd900503, 1999.
Pappalardo, G., Wandinger, U., Mona, L., Hiebsch, A., Mattis, I., Amodeo, A., Ansmann, A., Seifert, P., Linné, H., Apituley, A., Alados Arboledas, L., Balis, D., Chaikovsky, A., D'Amico, G., De Tomasi, F., Freudenthaler, V., Giannakaki, E., Giunta, A., Grigorov, I., Iarlori, M., Madonna, F., Mamouri, R.-E., Nasti, L., Papayannis, A., Pietruczuk, A., Pujadas, M., Rizi, V., Rocadenbosch, F., Russo, F., Schnell, F., Spinelli, N., Wang, X., and Wiegner, M.: EARLINET correlative measurements for CALIPSO: First intercomparison results, J. Geophys. Res., 115, D00H19, doi: 10.1029/2009jd012147, 2010.
Sasano, Y., Browell, E. V., and Ismail, S.: Error caused by using a constant extinction/backscattering ratio in the lidar solution, Appl. Opt, 24, 3929, doi: 10.1364/ao.24.003929, 1985.
Sugimoto, N., Matsui, I., Shimizu, A., Uno, I., Asai, K., Endoh, T., and Nakajima, T.: Observation of dust and anthropogenic aerosol plumes in the Northwest Pacific with a two-wavelength polarization lidar on board the research vessel Mirai, Geophys. Res. Lett., 29, 1901, doi: 10.1029/2002gl015112, 2002.
Tesche, M., Wandinger, U., Ansmann, A., Althausen, D., Müller, D., and Omar, A. H.: Ground-based validation of CALIPSO observations of dust and smoke in the Cape Verde region, J. Geophys. Res. Atmos., 118, 2889-2902, doi: 10.1002/jgrd.50248, 2013.
Wandinger, U., and Ansmann, A.: Experimental determination of the lidar overlap profile with Raman lidar, Appl. Opt., 41, 511-514, doi: 10.1364/AO.41.000511, 2002.
Wang, Z., Huang, X., and Ding, A.: Optimization of vertical grid setting for air quality modelling in China considering the effect of aerosol-boundary layer interaction, Atmos. Environ., 210, 1-13, doi: 10.1016/j.atmosenv.2019.04.042, 2019.
Whiteman, D., Melfi, S., and Ferrare, R.: Raman lidar system for the measurement of water vapor and aerosols in the Earth's atmosphere, Appl. Opt., 31, 3068-3082, doi: 10.1364/AO.31.003068, 1992.
Winker, D. M., Vaughan, M. A., Omar, A., Hu, Y., Powell, K. A., Liu, Z., Hunt, W. H., and Young, S. A.: Overview of the CALIPSO Mission and CALIOP Data Processing Algorithms, J. Atmos. Oceanic Technol., 26, 2310-2323, doi: 10.1175/2009jtecha1281.1, 2009.

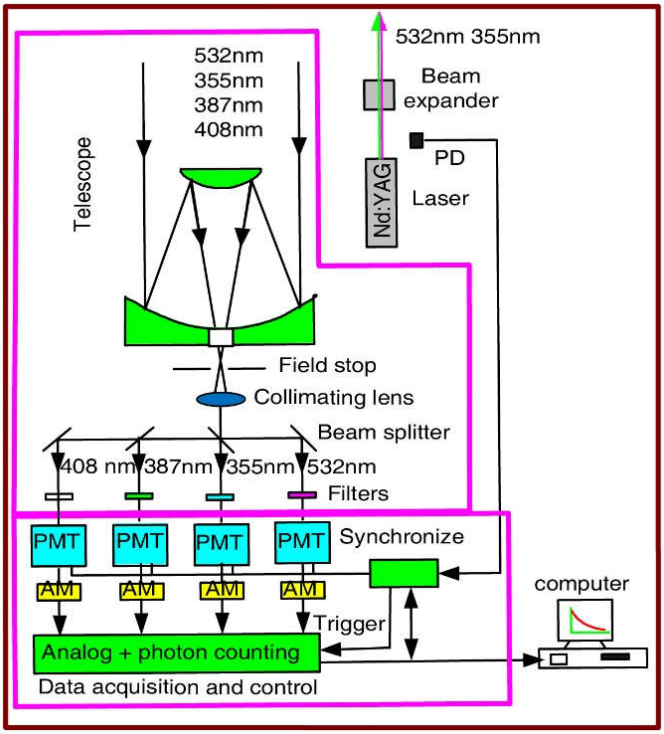

Figure S1. Schematic of multi–wavelength polarization RL system.

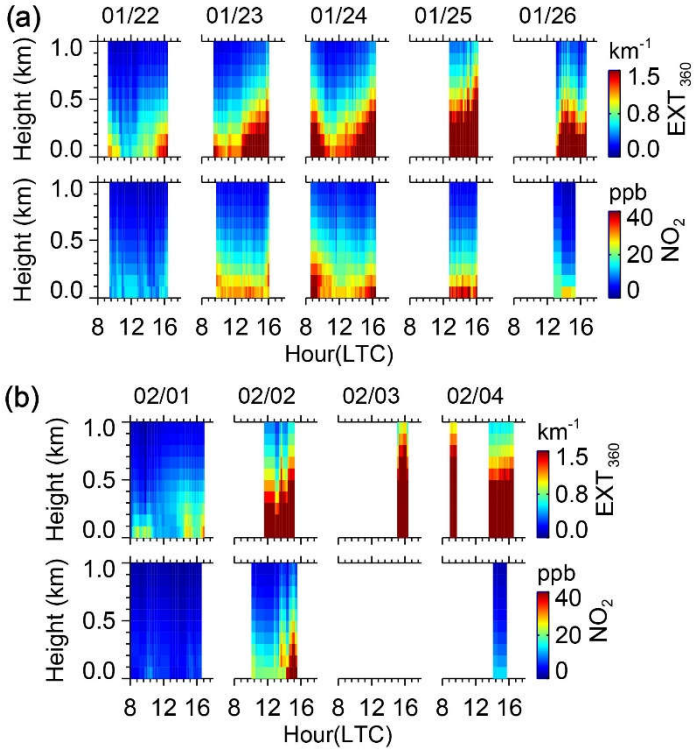

Figure S2. Curtain plots of MAX–DOAS observations. (**a**) EXT_{360} and NO_2 VMR from 22 to 26 Jan 2017, (**b**) EXT_{360} and NO_2 VMR from 1 to 4 Feb 2017.

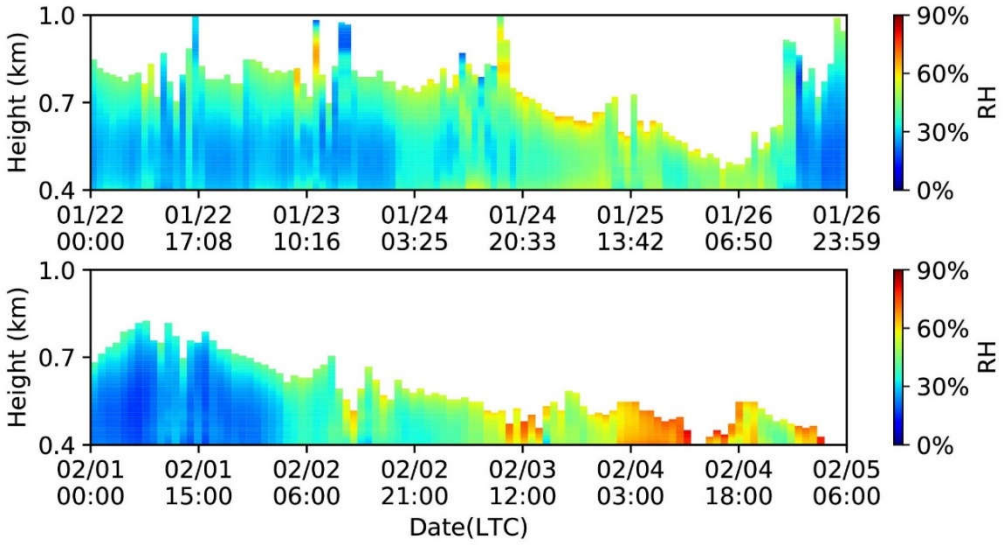

Figure S3. Curtain plots of relative humidity during HPI 1 and HPI 2.

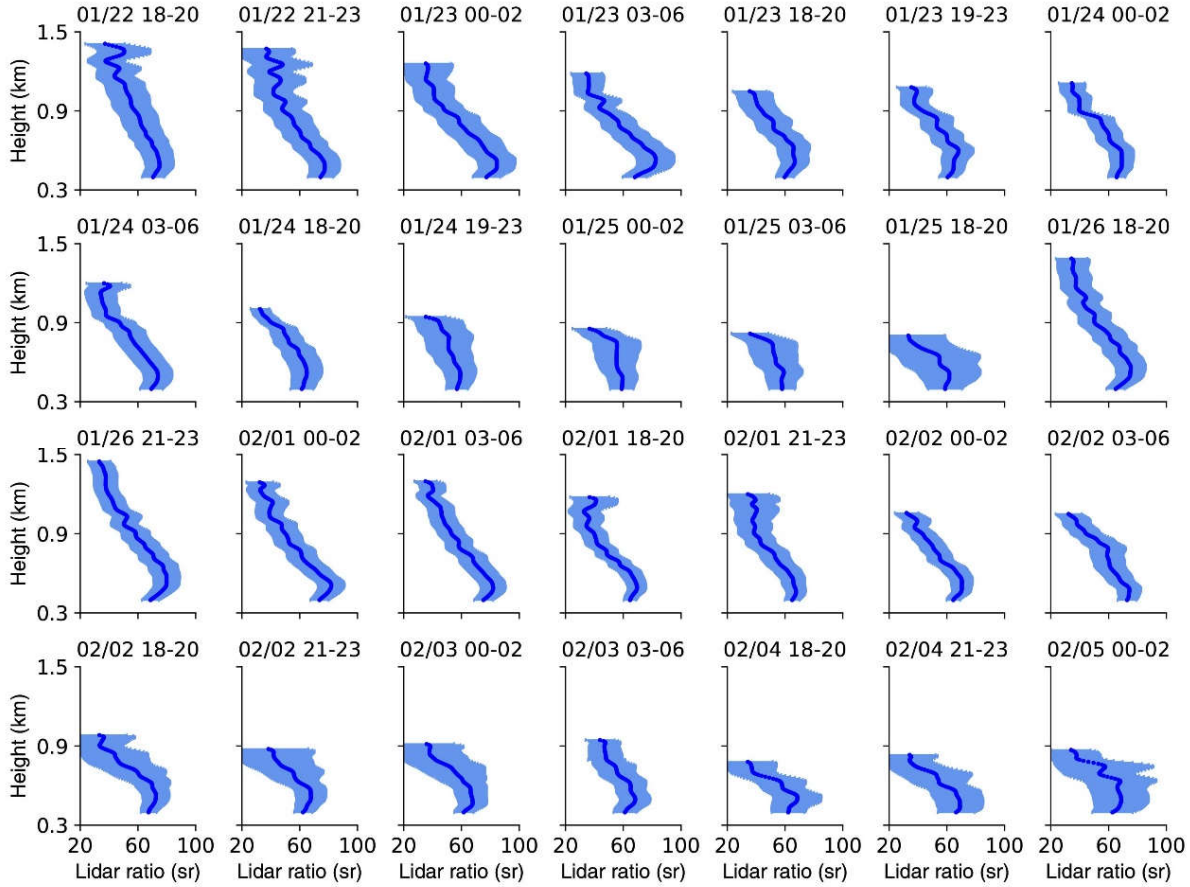

Figure S4. Lidar ratio profiles at 355 nm measured during HPI 1 and HPI 2. Three–hour average LR profile is the thick blue line and the envelope represents the errors at each altitude. The time (LTC) of each profile is displayed at the top of each panel. Error bars are calculated from the law of error propagation, which primarily depends on the signal–to–noise ratio (Heese et al., 2010) of the input signal given in Table 2.

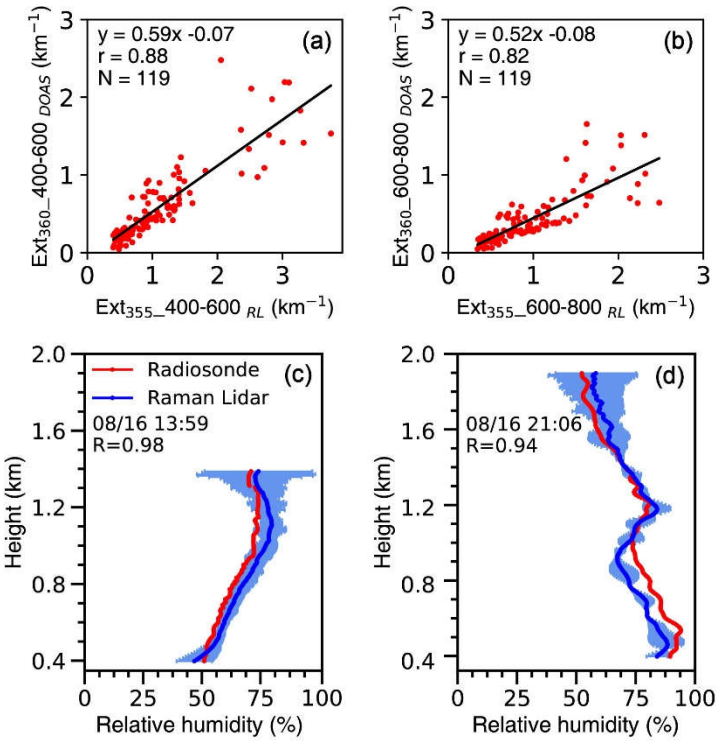

Figure S5. Data comparison of RL and MAX–DOAS. Correlations between EXT from MAX–DOAS and RL for layers of (**a**) 400–600 m and (**b**) 600–800 m. RH comparison between radiosonde and RL at (**c**) noon and (**d**) night. The envelopes in (**c**) and (**d**) represent the errors at each altitude. The error is calculated from the law of error propagation, which primarily depends on the signal–to–noise ratio (Heese et al., 2010) of the input signal given in Table 2.

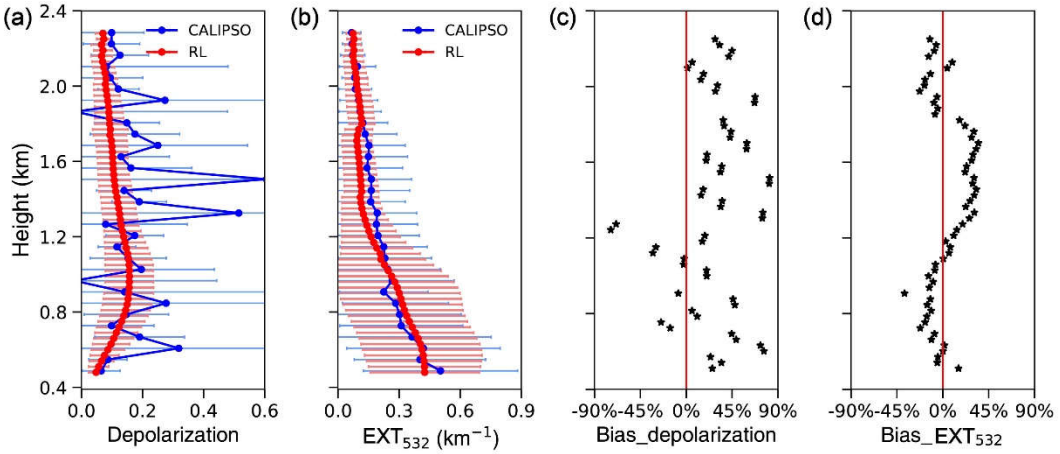

Figure S6. Comparison of average depolarization ratio and EXT_{532} between RL and CALIPSO over Jan to Mar 2017. (**a**) Comparison of VDR measured by RL and PDR measured by CALIPSO, (**b**) EXT_{532} comparison measured by CALIPSO and RL. The envelope over the horizontal bars in (**a**) and (**b**) represents one standard deviation at each altitude. The relative bias of depolarization and EXT_{532} compared with RL and CALIPSO are shown in (**c**) and (**d**), respectively.

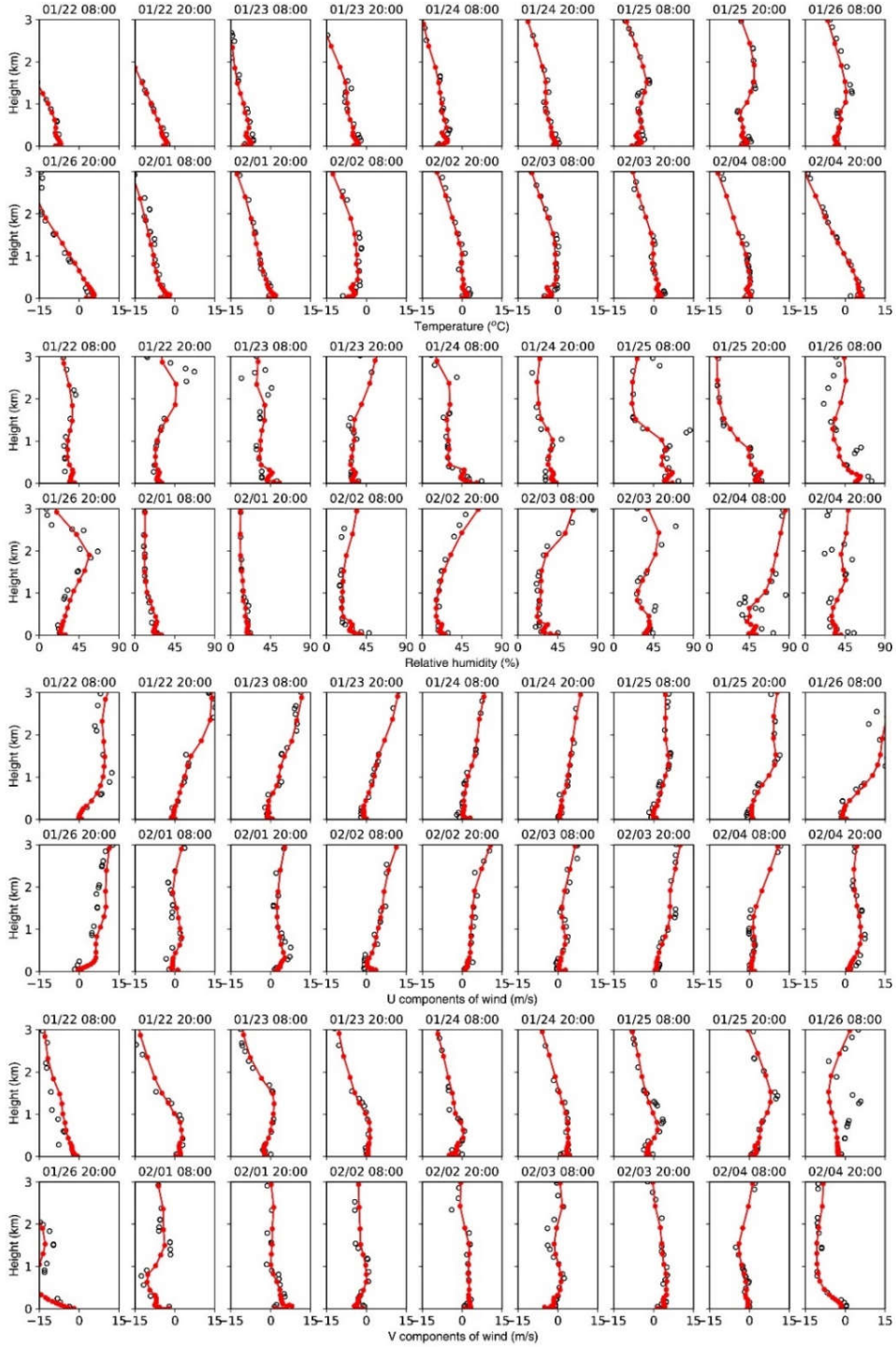

Figure S7. Comparison of WRF–Chem simulations (red dots) and observations (black dots). Comparison of the vertical profiles of temperature, vertical profiles of relative humidity, vertical profiles of wind speed (u components), and vertical profiles of wind speed (v components) between simulations and observations.

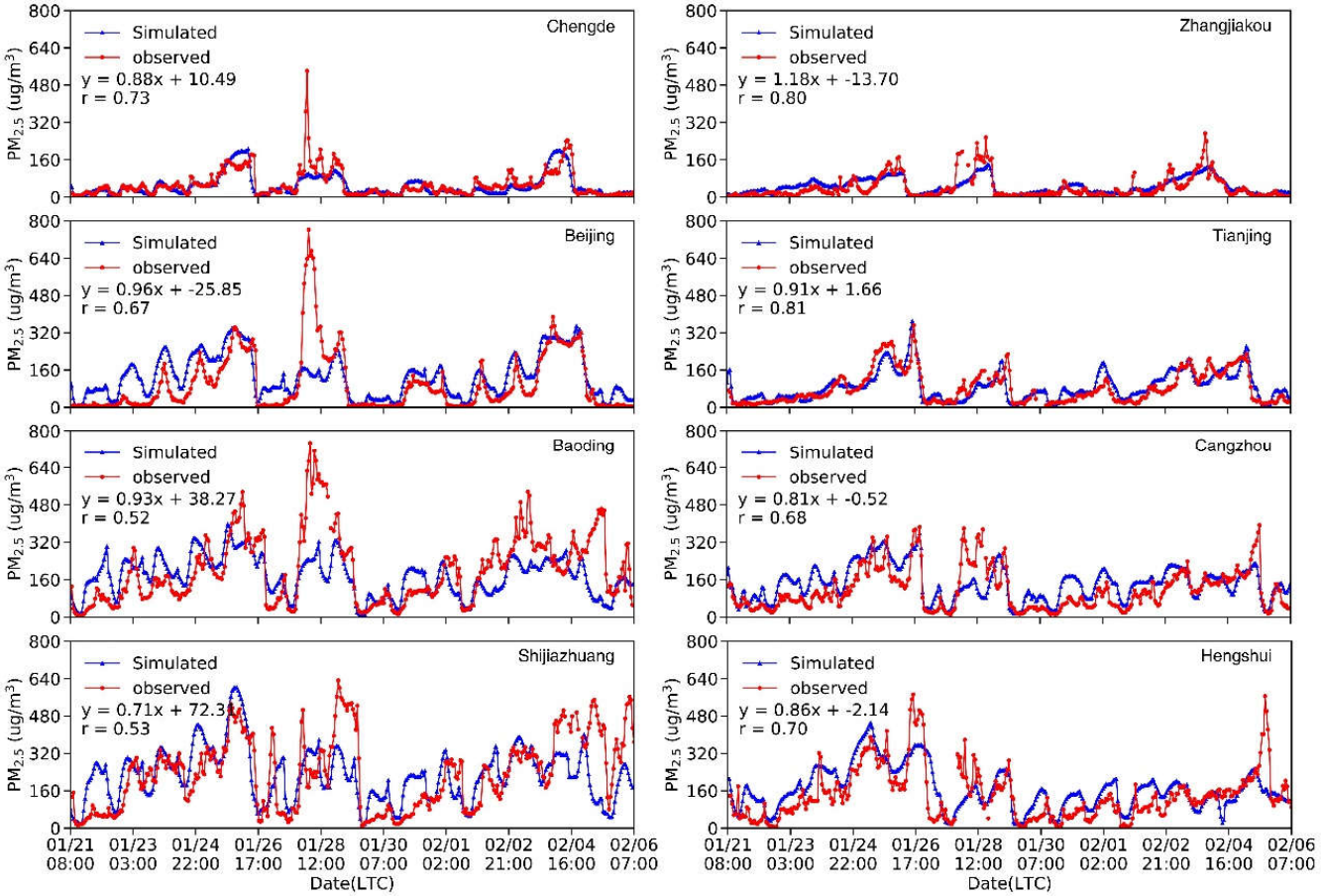

Figure S8. Comparison of simulated and observed $PM_{2.5}$ during the whole observation. Time series of the observed (red dots) and simulated (blue triangle) hourly $PM_{2.5}$ concentrations ($\mu g/m^3$) in the eight cities (Chengde, Zhangjiakou, Beijing, Tianjing, Baoding, Cangzhou, Shijiazhuang and Hengshui) from 21 Jan to 6 Feb 2017.

Table S1. CALIPSO overpasses (within 150 km distance) used for comparison during our observation period.

Date	Time (UTC)	Separation (km)
23 Jan	1813	51
1 Feb	1808	83
2 Feb	0448	144
8 Feb	1815	51
9 Feb	0454	14
17 Feb	1809	83
18 Feb	0449	144
24 Feb	1816	53
25 Feb	0456	13
5 Mar	1811	83
6 Mar	0451	144
12 Mar	1838	49
21 Mar	1813	88
28 Mar	1820	46
29 Mar	0500	8